NASA TECHNICAL NOTE

NASA TN D-4215

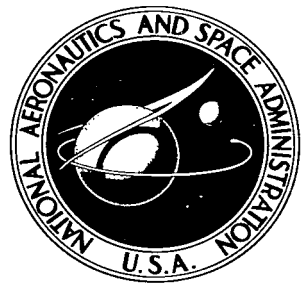

NASA TN D-4215

DYNAMIC MODEL INVESTIGATION OF TOUCHDOWN STABILITY OF LUNAR-LANDING VEHICLES

by Robert W. Herr and H. Wayne Leonard

Langley Research Center
Langley Station, Hampton, Va.

NATIONAL AERONAUTICS AND SPACE ADMINISTRATION • WASHINGTON, D. C. • OCTOBER 1967

NASA TN D-4215

DYNAMIC MODEL INVESTIGATION OF TOUCHDOWN STABILITY OF LUNAR-LANDING VEHICLES

By Robert W. Herr and H. Wayne Leonard

Langley Research Center
Langley Station, Hampton, Va.

NATIONAL AERONAUTICS AND SPACE ADMINISTRATION

For sale by the Clearinghouse for Federal Scientific and Technical Information
Springfield, Virginia 22151 – CFSTI price $3.00

DYNAMIC MODEL INVESTIGATION OF TOUCHDOWN STABILITY OF LUNAR-LANDING VEHICLES

By Robert W. Herr and H. Wayne Leonard
Langley Research Center

SUMMARY

A 1/6-scale dynamic model of a lunar module (LM) type of spacecraft has been tested to determine the overturning stability boundaries for landings on nonlevel surfaces. The model has four inverted tripod legs with aluminum honeycomb shock absorbers in each leg strut. Experimental stability boundaries have been compared with analytical boundaries derived from three different mathematical idealizations of the model: a rigid, nondeformable model; a rigid model with shock absorbers; and an elastic model with shock absorbers utilizing measured model characteristics as inputs to the analyses. The data are used to illustrate the effects of vehicle shock-absorbing action and overall vehicle elastic properties on landing stability. Effects on vehicle landing stability of variations in vehicle velocity, orientation, and the magnitude and direction of the surface slope are shown both experimentally and analytically.

In general, it was found that accurate analytical prediction of the critical approach velocities based on overturning stability requires that the analysis include both the model elasticity and shock-absorber characteristics. Further, it was observed that approach yaw angles which result in three-dimensional post-impact tumbling motions can impose severe limitations on landing-approach velocities.

INTRODUCTION

Among the problems associated with placing a manned vehicle on the lunar surface is that of assuring that the spacecraft will not overturn upon landing. This assurance of landing stability requires an understanding of the general tumbling motions which may result when a multi-legged vehicle impacts on a surface whose topography and consistency are as yet not well defined.

Several organizations have studied this problem, and they generally rely on dynamic-model tests with supporting analysis. Such studies are illustrated in references 1 to 6. This early work was based upon the assumption that symmetrical

approaches resulting in two-dimensional tumbling were the most critical landing conditions with respect to overturning stability. It was shown, however, in reference 7 that for simple, rigid models, asymmetrical approach attitudes which result in three-dimensional tumbling can impose more severe limitations on approach velocities and landing site slopes than symmetrical landings.

Neither the model nor the supporting analysis used in reference 7 considered the effects of shock absorbers or vehicle elasticity. Consequently, a research program was initiated at the Langley Research Center to define the dynamic behavior of a more realistic, multi-legged elastic vehicle equipped with shock absorbers and subjected to asymmetrical landings on an inclined rigid surface. This research program was conducted in two separate but coordinated parts. In the experimental phase of the program reported herein, a model, similar to and about one-sixth the size of the lunar module (LM) configuration, was utilized to generate landing stability boundaries. In the second phase, an analysis was performed in which the equations of motion of a generalized vehicle were written and programed for solution on a digital computer. The analysis and associated computer program are presented in reference 8.

This paper presents a description of the model and experimentally determined landing stability boundaries. These experimental data are then used as a check on the accuracy of stability boundaries derived from the analyses of reference 7 for a rigid, nondeformable model and of reference 8 for a rigid model with shock absorbers and for an elastic model with shock absorbers. The results are used to illustrate the effects of vehicle physical properties, approach orientation, and landing-surface slopes on landing stability.

SYMBOLS

F	force, lb (newtons)
K	spring rate, pounds/foot (newtons/meter)
V_h	horizontal velocity component, feet/second (meters/second)
V_V	vertical velocity component, feet/second (meters/second)
d	deflection, feet (meters)
α_s	cross-slope angle, degrees

ψ_s yaw angle measured from direction of downhill slope, degrees

σ landing surface slope, degrees

DESCRIPTION OF APPARATUS

General

Experimentally determined landing stability boundaries were obtained by using the model shown in figure 1. A simple, four-bar parallel linkage or trapeze was used to launch the model onto an inclined surface. The general configuration of the model landing gear and the model mass and dimensional properties were derived from an early engineering version of the LM spacecraft. To make the foot-ground interaction more controllable, the foot pads used on the full-scale spacecraft were replaced by spikes which were stopped abruptly by a plywood surface but were free to lift off. This condition generally results in a more critical landing from a stability standpoint than when impacting on a moderately soft or slippery surface. The shape of the model body was not intended to simulate the spacecraft configuration since its only function is to support the model landing gear and ballast weights. The model is nominally one-sixth size of a full-scale LM vehicle. Velocities associated with model tests under earth gravity are therefore identical to velocities associated with a similar full-scale vehicle under lunar gravity. Scaling is of no real importance, however, since the primary purpose of the experiments was to provide a check on the accuracy of the analytical procedures and results.

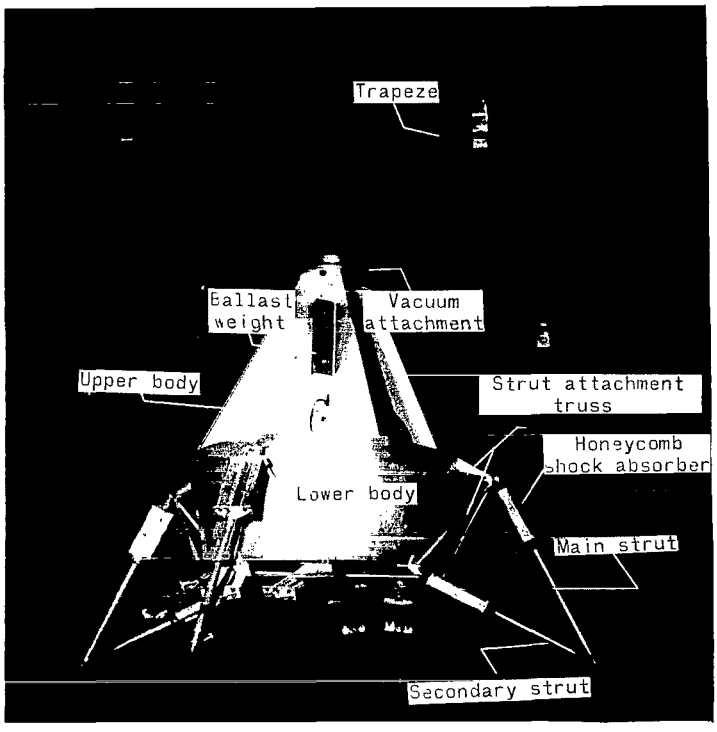

(a) Overall view of model and launch trapeze. L-64-8103.1

Figure 1.- Photographs of 1/6-scale model.

Model Construction Details

Body.- Construction of the model body section is illustrated in figure 1. Strut attachment trusses are fastened to the lower body section which is an aluminum conic frustum. The upper diameter of the frustum is 28 inches. The basic shell is longitudinally and circumferentially stiffened and is radially supported at each strut attachment point. Radial supports are connected to either end of a tube extending along the body center line. A pair of plates in the form of isosceles trapezoids make up the upper body. The plates are joined to form a cruciform structure. This portion of the model functions as a support for instrumentation and for ballast weights used to control the center-of-gravity location, mass, and mass moments of inertia. A flat plate, 10 inches in diameter, is attached to the top of the cruciform structure. This plate provides a mating surface for a vacuum attachment device which is used on the drop rig as a positive-hold, quick-release, model launch mechanism.

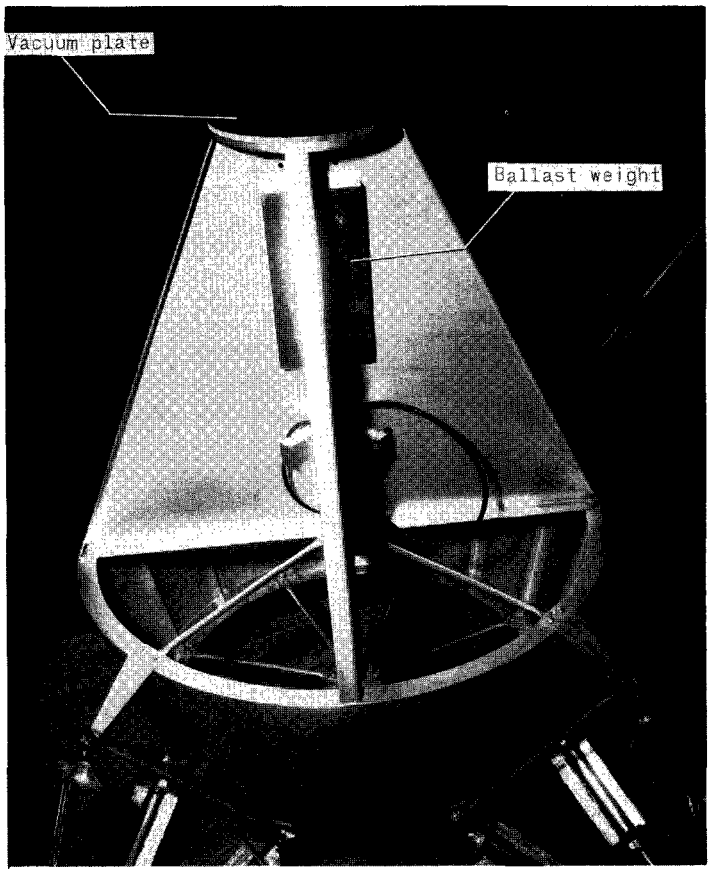

(b) View of upper body. L-64-8104.1

Figure 1.- Continued.

Landing gear.- The model landing gear consists of four, identical, symmetrically placed, leg assemblies. Each leg assembly is made up of three struts joined to form an inverted tripod terminating in a spike foot. All struts are tubular, telescoping devices containing shock absorbers. Each of the three struts is attached to the attachment truss by a universal or swivel joint. For clarity, the upper strut is referred to as the main strut and the two lower struts are called secondary struts. The spike foot is an integral part of the main strut as illustrated in the photographs in figure 2. Secondary struts are attached to the main strut at a point just above the spike. The swivel attachment fittings are shown in figure 2 before and after the gear assembly. Use of swivel or universal

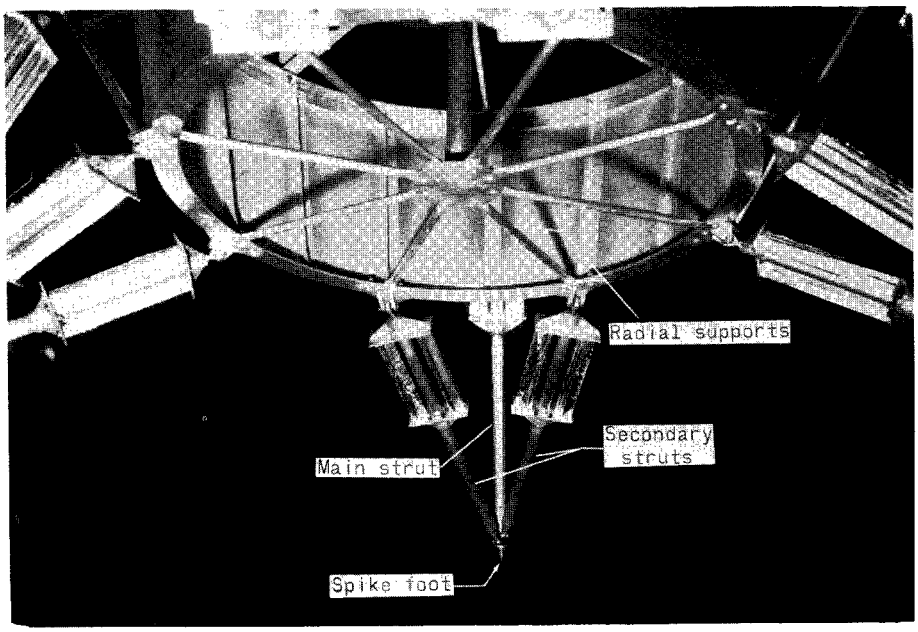

(c) Lower body and struts. L-64-8106.1

Figure 1.- Concluded.

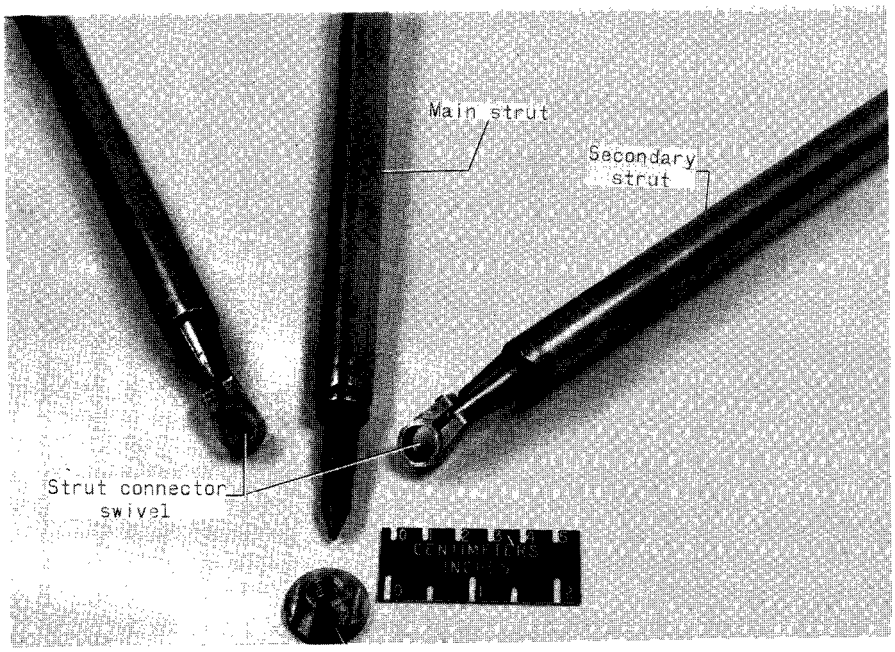

(a) Unassembled. L-66-2808.1

Figure 2.- Details of strut juncture.

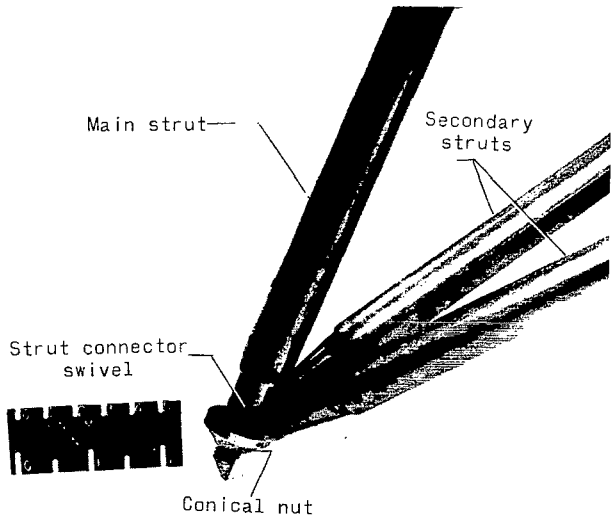

(b) Assembled. L-66-2809.1

Figure 2.- Concluded.

strut attachment, in conjunction with the telescoping properties of each assembly, gives considerable freedom of motion to each foot relative to the body.

Figure 3 is a drawing of the assembled strut showing the relative positions of the assembled parts and the lower end configurations for main and secondary struts. Figure 4 is an exploded view photograph of actual strut hardware. The upper portion of each strut was fabricated from 5/8-inch (2.6 mm) outside diameter aluminum tubing with an 0.049-inch (1.25 mm) wall. This section of the strut telescoped into the lower portion of the strut, a 3/4-inch (1.9 mm) outside diameter aluminum tube with an 0.035-inch (0.89 mm) wall. Bearing surface for this telescoping action was provided by teflon sleeve bearings positioned as shown in figures 3 and 4. The distance between bearings was approximately 4 inches (10.2 cm) with the strut fully extended and increased as the strut was telescoped. This arrangement resulted in a minimum of free play and showed no tendency to bind under simultaneous compression and bending loads. Compression strain gages, mounted on each strut, were monitored during the tests to assure that the bearings and shock absorbers functioned properly and that the struts did not bind.

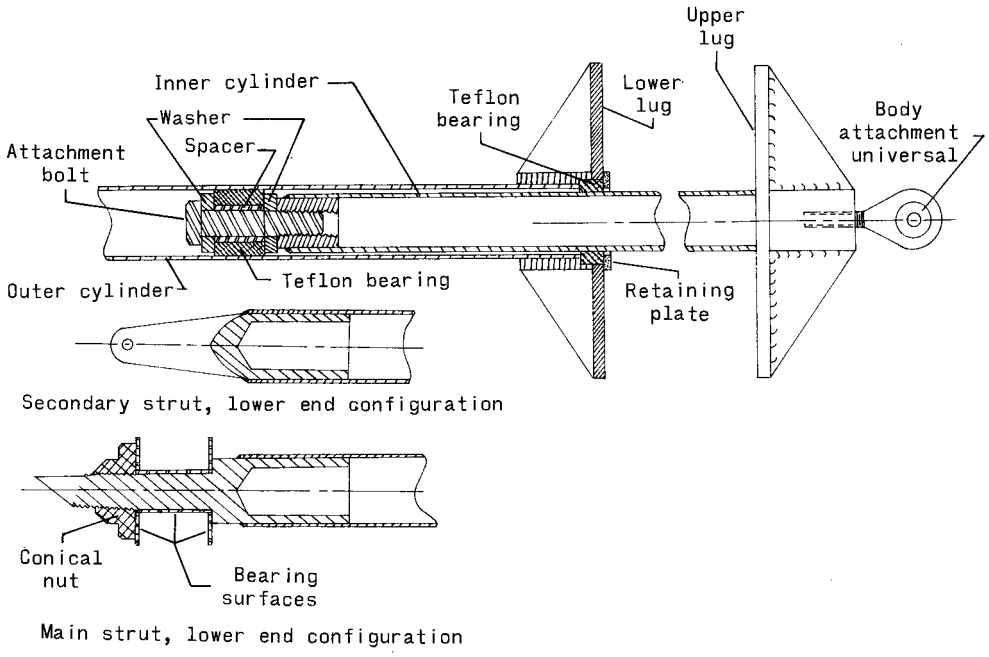

Figure 3.- Typical model strut assembly.

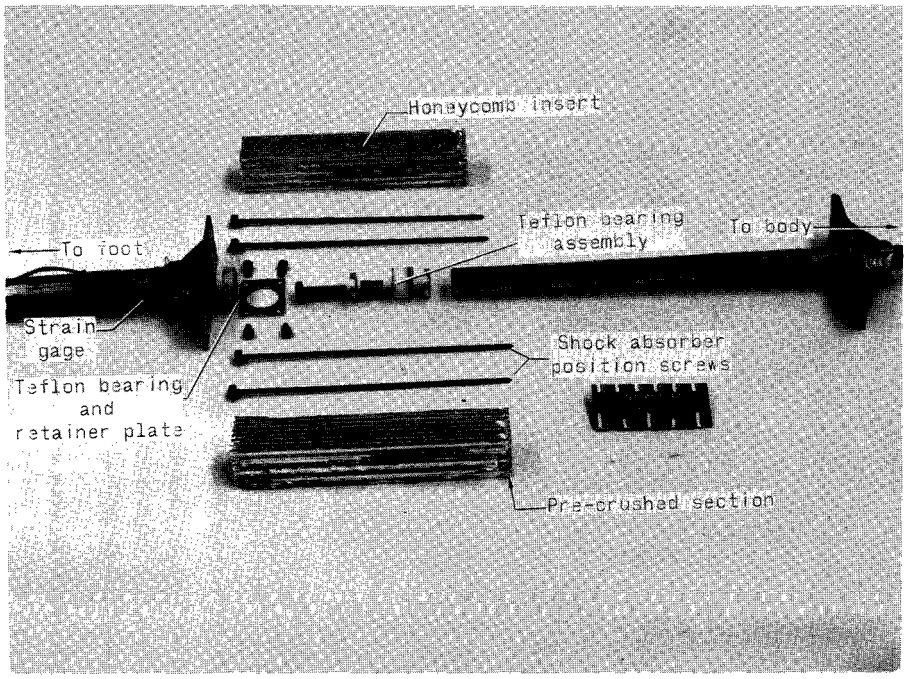

Figure 4.- Photograph of strut components. L-66-2811.1

For ease of assembly, the aluminum honeycomb shock absorbers were located externally between lugs welded to the struts as shown in figures 3 to 6. The 1/8-inch (3.2 mm), 0.0007 inch (1.8×10^{-2} mm) cell wall hexagonal cell honeycomb, used in all tests had a dynamic crush strength of 128 psi (8.82×10^5 N/m^2). Two 1-inch square (2.54 cm) cross-section honeycomb cartridges were used in each of the main struts to provide a constant 256 pounds (1140 N) force resisting compression stroking of each strut. Stroking of each secondary strut was resisted by two honeycomb cartridges each having a 0.71-inch square (1.7 cm) cross section and a resulting stroke load (compression only) of 128 pounds (570 N) per strut. Each cartridge was precrushed from an original length of 6 inches (15.2 cm) to $5\frac{1}{2}$ inches (14 cm) in order to eliminate the high force level necessary to initiate honeycomb buckling. The cartridges could be compressed to a length of 1 inch (2.54 cm) and thus a maximum strut stroke of $4\frac{1}{2}$ inches (11.4 cm) is allowed. The precrushed section of the honeycomb is visible in the photographs in figure 4.

As illustrated in figure 5, each cartridge was held in place by two long slender screws which were inserted through clearance holes in the lower lug, through the honeycomb cell opening, and threaded into the upper lug. Figure 5 shows one cartridge in place with the second cartridge removed for clarity. The cartridge-retaining screws also served as strut extension stops and prevented rotation of the lugs relative to each

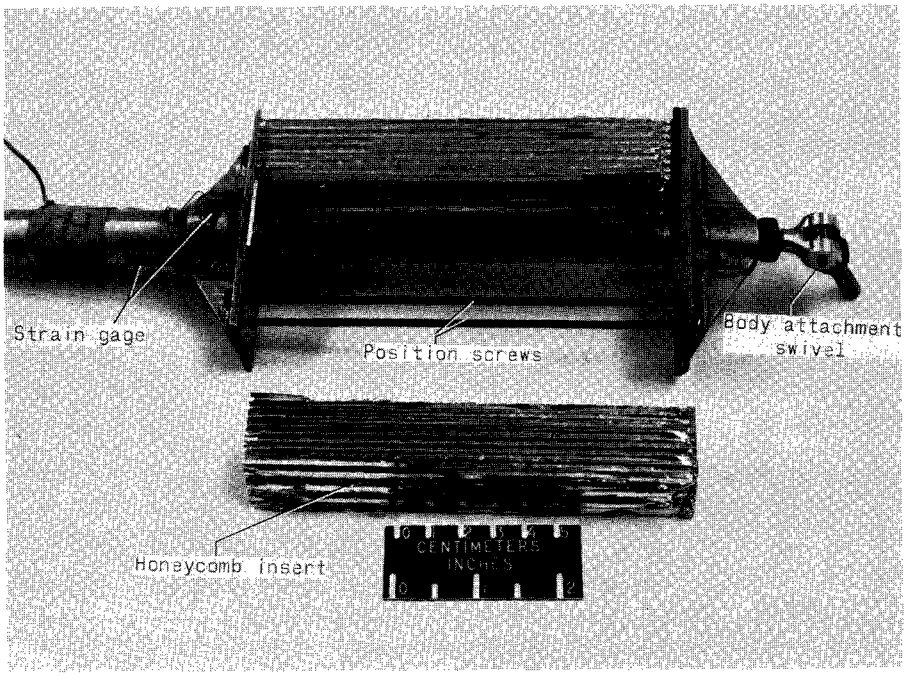

Figure 5.- Energy absorber with one cartridge removed. L-66-2810.1

other. Typical shock-absorber action is illustrated in figure 6 where the shock-absorber assembly is shown before and after strut stroking.

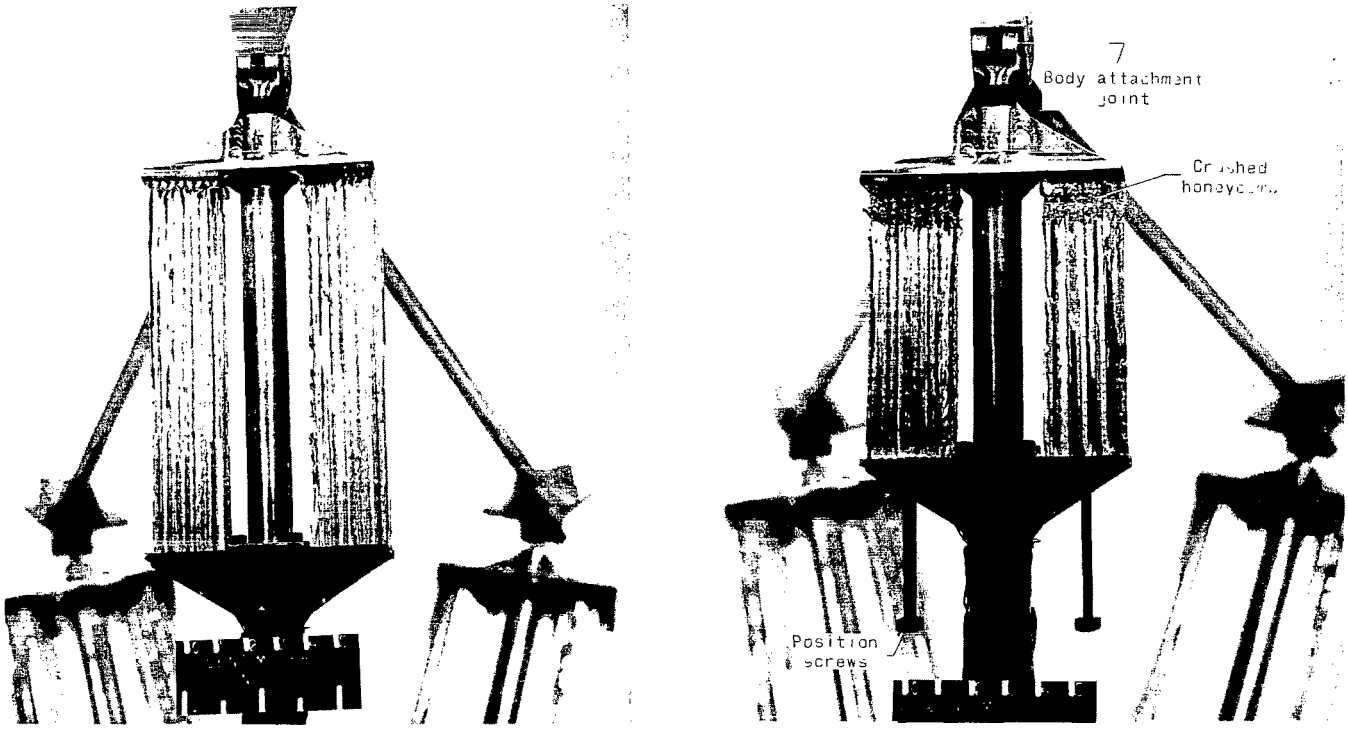

(a) Before impact. L-66-2813.1 (b) After impact. L-66-2812.1

Figure 6.- Energy absorber.

The true lengths of the undeformed struts are shown in figure 7. Also given in this figure are the measured model mass and mass moments of inertia about the center of gravity.

Launch Trapeze and Impact Platform

The model was launched from a four-bar pendulum, or trapeze, a portion of which is visible in figure 1. The purpose of the trapeze is to launch the model in a given direction and with controlled horizontal and vertical impact velocity components. Parallel linkages assure zero initial rotation rates. Model and trapeze were connected through a vacuum seal between the plate on top of the model and a mating plate with an 0-ring seal on the trapeze. Upon release, the model followed a ballistic trajectory to the point of impact. Forward velocity was controlled by the angle through which the

Mass moments of inertia about center of gravity		
	slug-ft^2	kg-m^2
Pitch	2.08	2.82
Roll	2.08	2.82
Yaw	1.10	1.49

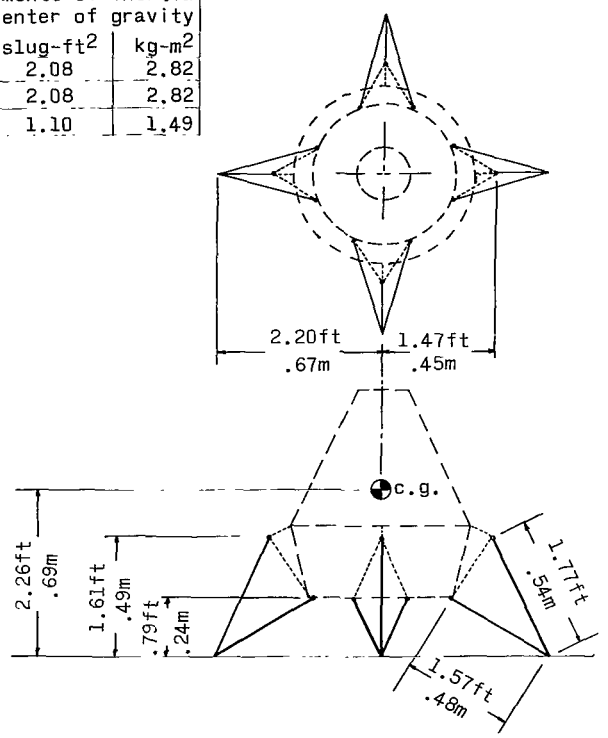

Figure 7.- Dimensional, mass, and inertial properties of 1/6-scale model.
Mass = 1.66 slug (24.23 kg)

pendulum was displaced from the bottom-dead-center release point and the vertical velocity was determined by the free-fall distance of the model from release to impact.

The impact platform consisted of a 5-ton (4535 kg) slab of reinforced concrete measuring 12 feet by 16 feet (3.66 m by 4.88 m). One end of the platform was pinned to a concrete floor and the other end could be elevated to provide the desired landing surface slope. The entire surface of the platform was covered with 3/4-inch (1.9 cm) plywood sheet.

TEST PROCEDURE

Both model and trapeze were swung as a unit until at bottom dead center of the swing, the vacuum seal was broken and the model continued in free-fall to impact the surface. For all tests reported herein, initial contact of the model with the landing surface was made with the model in a level attitude and with zero pitch, yaw, and roll rates. Landing-surface slopes were either 10° or 15°. For each set of test points used to determine a point on the stability boundary curve, all test variables were held

constant, except the vertical impact velocity which was incrementally increased until the model overturned. High-speed movies were made during selected test runs to aid in the study of the model behavior during impact.

RESULTS AND DISCUSSION

Experimental Results

Vertical landings on 15° slope.- The experimental stability profile in figure 8 was obtained by dropping the model vertically onto a 15° slope. The vertical impact velocity V_V is plotted for tests at various yaw angles ψ_S measured with respect to the direction of downhill slope. It should be noted that the points presented are only those between which changes in vehicle stability occurred since several tests at each yaw orientation were usually required to define the transition from stable to unstable to the nearest foot per second.

Vertical drops at $\psi_S = 0°$ and $\psi_S = 45°$ result in two-dimensional tumbling motions referred to, respectively, as 1-2-1 and 2-2 modes of overturning. In the 1-2-1 mode, the uphill foot makes initial contact with the surface and is followed in turn by a simultaneous impact of the two center feet and then the downhill foot. In the 2-2 mode, two uphill feet impact simultaneously and then the two downhill feet impact

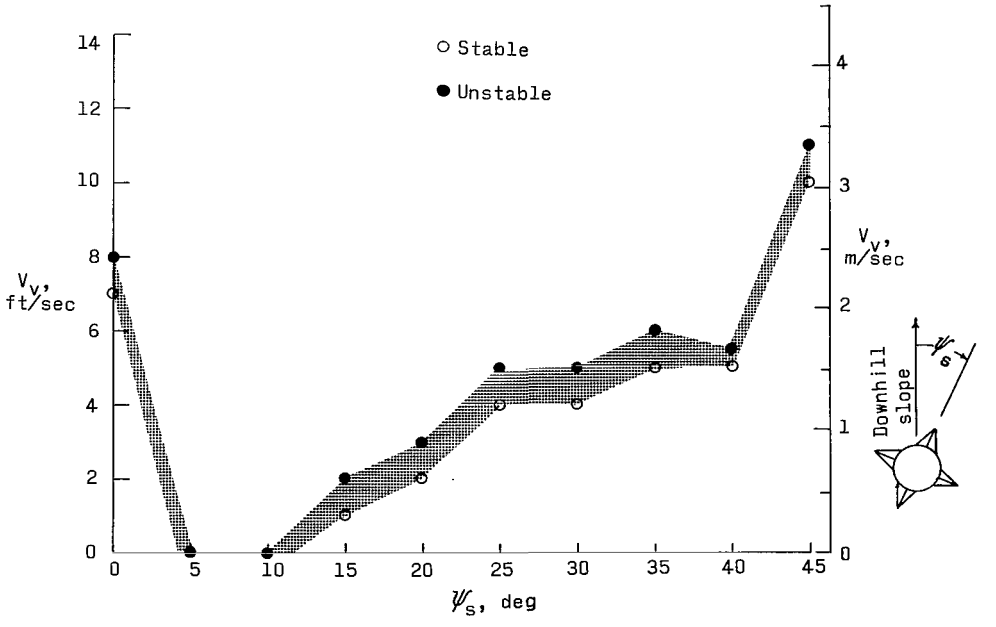

Figure 8.- Experimental stability profile-vertical velocity as a function of yaw orientation relative to direction of slope. $\sigma = 15°$; $V_h = 0$.

simultaneously. Intermediate values of $0^{o} < \psi_{s} < 45^{o}$ result in three-dimensional or asymmetric tumbling motions.

The figure shows that the symmetric 1-2-1 landing $\left(\psi_{s} = 0^{o}\right)$ is somewhat less stable than the symmetric 2-2 landing $\left(\psi_{s} = 45^{o}\right)$. Intuitively, it might seem that the reverse would be true since the 1-2-1 mode of overturning requires the expenditure of more kinetic energy to lift the model center of gravity to a point directly over the front foot. Since for rigid body impacts, the angular momentum after impact is equal to the moment of the momentum vector before impact, it follows that the vehicle will retain relatively more energy after the initial impact in a 1-2-1 approach than it would retain in a 2-2 impact. After initial impact in the 1-2-1 mode, the vehicle rotates about the rear foot until the two side feet strike the surface simultaneously. At this second impact the momentum vector lies well above and ahead of a line connecting the side feet so that, again, a high angular momentum and thus a large amount of kinetic energy is retained by the model. In contrast, the momentum vector will pass relatively close to the front feet during the second impact in a 2-2 mode; as a result, there is a greater loss of energy. As a matter of fact, if the center of gravity is sufficiently low relative to the tread radius, the momentum vector will fall behind a line connecting the two front feet, and the vehicle will have no tendency to overturn regardless of the magnitude of the impact velocity.

Another striking aspect of the data is that the stability boundary in the intermediate yaw angle regions is considerably lower than that for either of the two symmetric cases. This general trend, obtained from a model equipped with shock absorbers, is consistent with both the experiment and analysis presented in reference 7 which were obtained from a small rigid model. This degradation of landing stability is shown to be severe as the model is yawed from the 1-2-1 mode $\left(\psi_{s} = 0^{o}\right)$. At yaw orientations of 5^{o} and 10^{o}, the model was unstable at $V_{v} = 0$. This abrupt drop in the stability boundary made the experimental 1-2-1 mode extremely difficult to obtain. Slight errors in model orientations cause the model to fall off to one side or the other. Although not as precipitous, the results show that a marked reduction in stability occurs as the model is yawed from the 2-2 mode $\left(\psi_{s} = 45^{o}\right)$.

Vertical landings on 10^{o} slope.- Test conditions for the data in figure 9 were identical to those for figure 8 with the exception of the landing surface slope which was reduced from 15^{o} to 10^{o}. As would be anticipated, the effect of this reduction in slope is to raise the stability boundary. Although the trends remain generally the same, the boundary does not drop as abruptly nor as far in the asymmetric regions near $\psi_{s} = 0^{o}$ and $\psi_{s} = 45^{o}$.

Landings with forward velocity on 10^{o} slope.- The effect of nonvertical descents on landing stability is illustrated by the data in figure 10 which show vertical impact

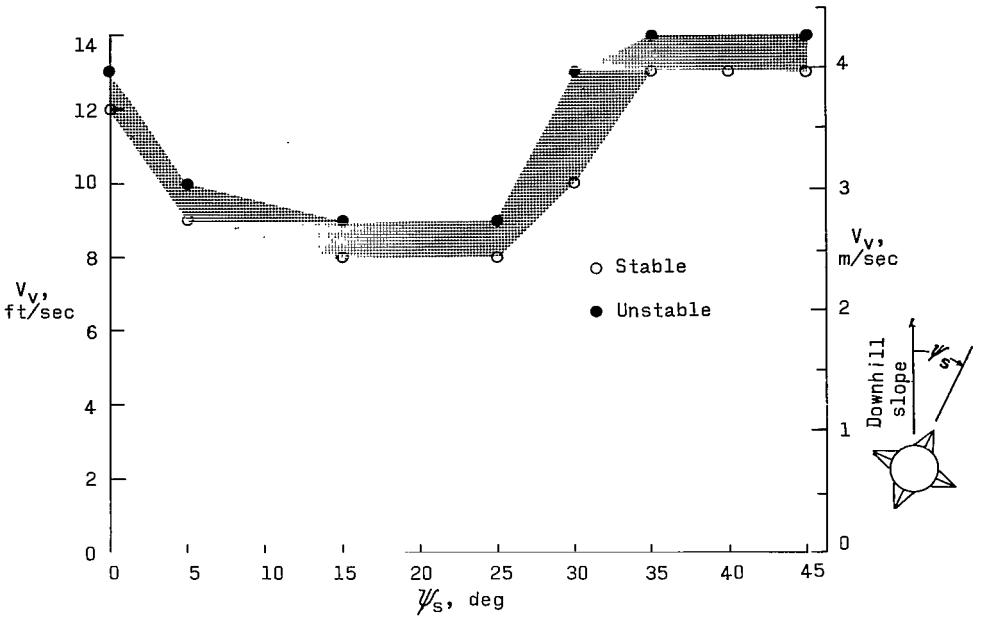

Figure 9.- Experimental stability profile-vertical velocity as a function of yaw orientation relative to direction of slope. $\sigma = 10^0$; $V_h = 0$.

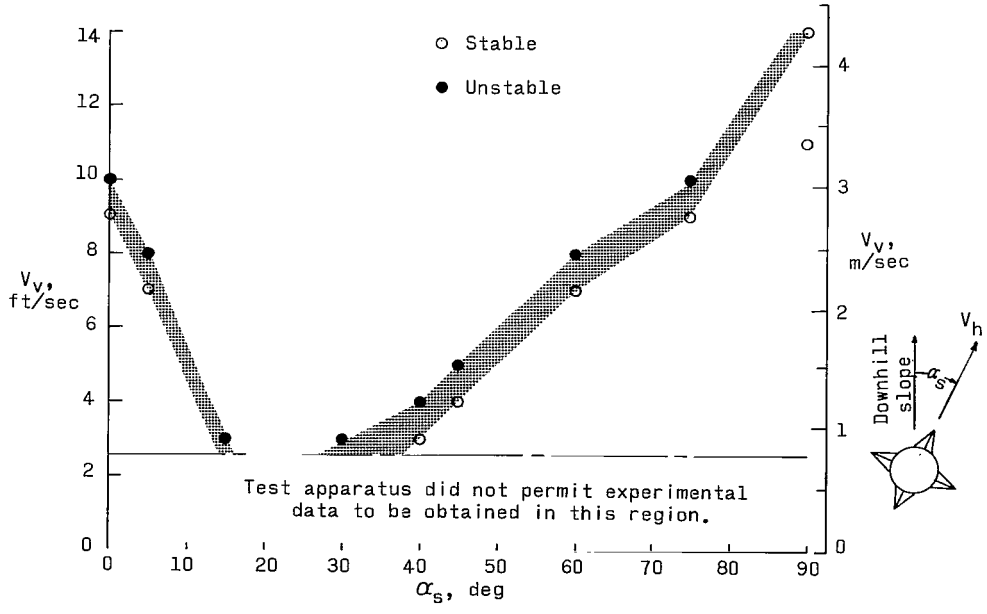

Figure 10.- Experimental stability profile-vertical velocity as a function of cross-slope angle. $\sigma = 10^0$; $V_h = 5$ ft/sec (1.74 m/sec); $\psi_s = 0$.

velocity V_v plotted against the cross-slope angle α_s for landings on a 10^o slope. The cross-slope angle, as defined in the sketch in figure 10, is the angle between the direction of downhill slope and the direction of the flight path or horizontal-velocity component. All cross-slope angles where $\alpha_s > 0$ result in asymmetrical post-impact tumbling. For these tests, the horizontal component of velocity V_h was maintained at 5 ft/sec (1.52 m/sec) while the vehicle yaw angle with respect to the flight path was maintained at zero, that is, the fore-and-aft feet were kept alined with the flight path.

Comparison of the data of figures 9 and 10 indicates that the presence of horizontal velocity tends generally to lower the stability boundary. It was not possible to define experimentally a transition region at the cross-slope angles from 15^o to 30^o since the model was unstable at the minimum drop height which could be attained in the test facility. At lower drop heights, the rear foot of the model contacted the landing surface during the downward swing of the trapeze. It was also not possible to define a transition region at $\alpha_s = 90^o$ since the model was stable at 14 ft/sec (4.26 m/sec) which is the maximum velocity attainable in the test facility.

Analytical Results

Stability boundaries as derived from three different mathematical representations of the model and experimentally determined model elastic properties are presented in figures 11 to 15. A comparison of the analytically determined boundaries with the previously shown experimental boundaries is given in figures 11, 14, and 15.

The data for the rigid-body boundaries were obtained by digital simulation of the model as described in reference 7. In this representation of the model, the body and landing gear are considered to be a rigid, nondeformable unit. For convenience in the numerical analysis of the problem, the ground was represented as a viscous surface in which foot penetration was impeded by a force proportional to the foot velocity but which did not resist lift-off. The data shown were computed with the value of the viscous constant selected to limit the maximum foot penetration to approximately 0.025 ft (7.3 mm) at an impact velocity of 14 ft/sec (4.26 m/sec).

The boundaries associated with inelastic and elastic shock absorbers were computed by using the analysis and associated computer program presented in reference 8. For the curves labeled inelastic shocks, the model was assumed to be rigid but the individual struts could undergo axial deformation or stroking which was opposed by a constant magnitude force. Compression stroking of each of the main struts was resisted by a constant 256 lb (1140 N) force and compression deformation of each secondary strut was resisted by a 128 lb (570 N) force. The extensional stroking of the struts was not permitted to exceed their original undeformed lengths. Extensional stroking, where permitted, was resisted by a 5 lb (22.2 N) force which corresponds to the maximum frictional

force measured on the model struts. The mathematical representation of the model identified by the term elastic shocks is similar to the inelastic shocks model with the exception of a spring in series with the shock absorber.

Vertical landings on 15° slope.- Computed stability boundaries for vertical landings with 15° landing surface slope are presented in figure 11. In the vicinity of the boundaries, computer runs were made at velocity increments of 0.5 ft/sec (15.2 cm/sec). The faired curves are thus accurate to within this value. Computer runs were made at 5° increments in the yaw orientation except in regions of abrupt change, in which case 1° increments were used as indicated in the inset of figure 11. Stable analytical points are denoted by a plus sign and unstable points by a minus sign.

For the symmetric 2-2 mode of overturning $(\psi_s = 45^o)$, the stability boundary as predicted by the rigid-body theory is shown to be lower than the experimental results by about 2 ft/sec (61.0 cm/sec). Fairly good agreement is obtained for the asymmetric landings in the range $25^o < \psi_s < 35^o$ but the rigid-body theory fails to predict the sharp dip in the measured stability boundary in the vicinity of $\psi_s = 10^o$.

It should be noted that for the special case of $\psi_s = 0^o$, the rigid body predictions have little practical significance because of the distortions of impact sequence caused by

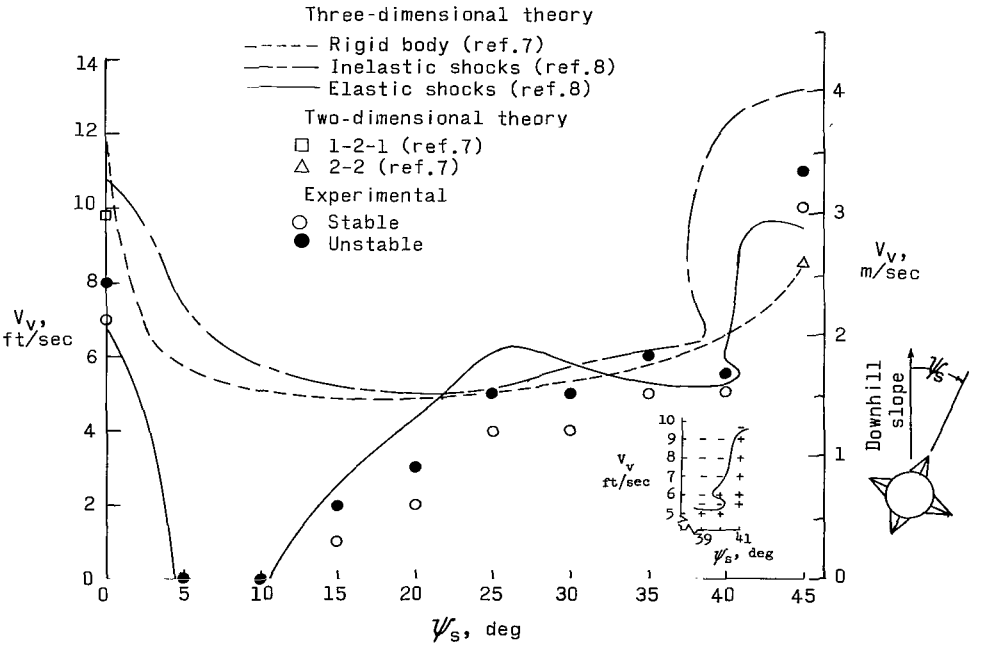

Figure 11.- Experimental and analytical stability profile-vertical velocity as a function of yaw orientation relative to direction of slope. $\sigma = 15^o$; $V_h = 0$.

the penetration of the surface which is permitted under the viscous ground assumptions. An impenetrable ground would result in a 1-3 mode wherein the uphill foot impacts, followed by a simultaneous impact of the remaining three feet. Since it would not be possible to determine the distribution of the forces acting on the feet, the stability characteristics of this mode are indeterminate. Penetration of the surface permitted by the viscous ground assumption results in the two side feet contacting the surface prior to the front foot impact or a 1-2-1 mode of overturning. The time lag between the impacts of the various feet, the magnitude and direction of the momentum vector prior to each impact, and consequently the stability characteristics, are dependent on the viscous constants assigned to the surface. It is, however, possible to evaluate the rigid-body behavior at $\psi_S = 0^o$ by use of the two-dimensional inelastic impact theory given in reference 7.

Stability boundaries were therefore manually computed by utilizing the procedures of reference 7 for both the 1-2-1 mode and the 1-0-1 mode wherein the side feet do not contact the surface. The transition points for the 1-2-1 mode thus calculated are shown in the figures as the square symbols and are shown to lie below the rigid-body theory points. The 1-0-1 calculation yields transition points nearly an order of magnitude higher than any of the other points and are not shown in the figures. As a check on the accuracy of the rigid-body theory at values of $\psi_S > 0^o$, the transition points predicted by two-dimensional inelastic impact theory for the 2-2 mode $(\psi_S = 45^o)$ were manually computed. The values thus determined were found to be in exact agreement with the rigid-body theory of reference 7 as shown by the triangular symbol at $\psi_S = 45^o$.

The landing stability boundaries predicted by the inelastic-shock-absorber representation of the model show no better agreement with the experimental results than do the rigid-body boundaries. The two theoretical curves are nearly coincidental throughout the middle range of yaw orientations; however, the inelastic-shock-absorber theory deviated from rigid-body theory at the higher values of ψ_S. The boundary computed by inelastic-shock-absorber theory rises abruptly at $\psi_S \approx 38^o$ to a value of about 13 ft/sec (3.96 m/sec) and maintains this value through $\psi_S = 45^o$. The inelastic-shock-absorber theory also fails to predict the sharp drop in the experimental stability boundary in the region of $\psi_S = 0^o$.

A clue to the poor correlation between the analyses and experiment for low values of ψ_S was provided by examination of the high-speed motion pictures which revealed that after the initial impact, the impacting foot would rebound briefly and experience one or more subsequent impact-rebound sequences before the second foot contacted the surface. In either the rigid-body or inelastic-shock-absorber analysis, a foot remains in contact with the surface until another foot impacts. It was thus clear that the model was storing elastic energy during the impact.

In order to obtain a gross approximation of the combined strut-body elastic characteristics, the model was statically loaded and the resultant deflection curves measured. Sketches of the static test setup and the load-deflection curves are shown in figures 12 and 13. To obtain the effective elasticity of the upper or main struts, all struts with the exception of two opposite main struts were removed from the model. Resting on these

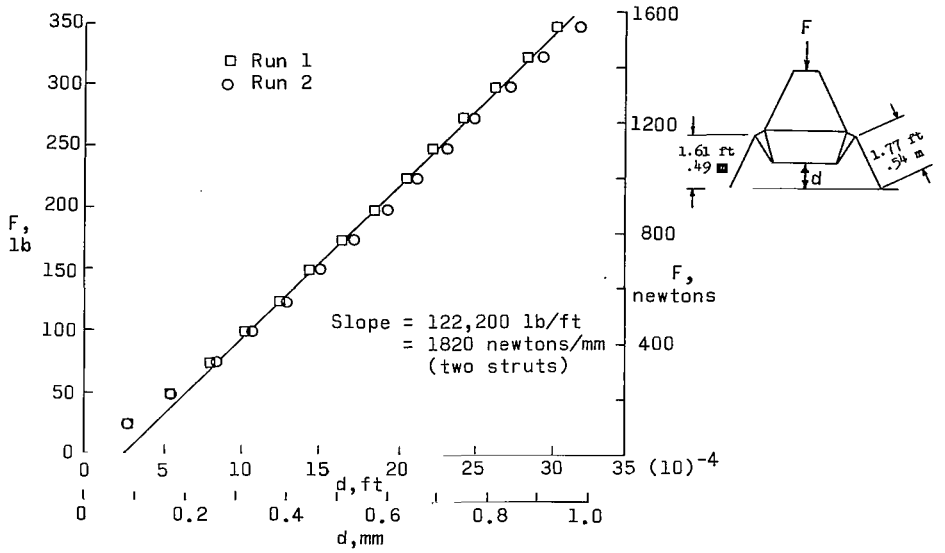

Figure 12.- Effective stiffness of body and main strut.

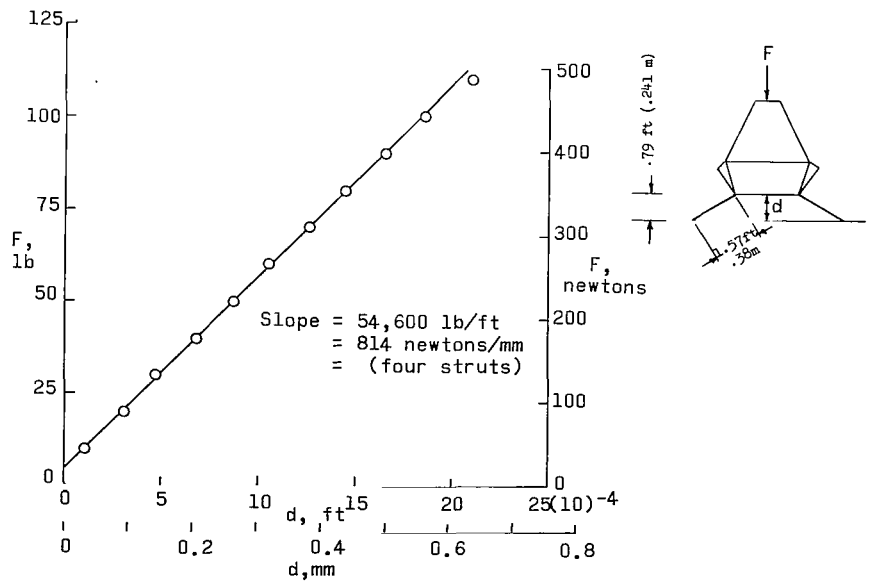

Figure 13.- Effective stiffness of body and secondary strut.

two struts, the model was restrained from lateral motion and statically loaded along the vertical center line through the vacuum plate. Model deflections were then measured at the center of the lower body. Since the model is relatively rigid along the center line, the deflections measured at the bottom of the model should be the same as the load-induced displacements at the load point. The resulting load-deflection curve is shown as figure 12. The combined body and strut spring rate defined by this curve was resolved into an effective spring constant according to the relation

$$K = \frac{122\,200}{2}\left(\frac{1.77}{1.61}\right)^2$$

$$K = 73\,900 \text{ lb/ft/strut}$$

$$K = 1100 \text{ newtons/mm/strut}$$

This spring acts along the axis of each of the main struts and in series with the shock absorber. The effective elasticity of the lower struts (fig. 13) was obtained according to the relation

$$K = \frac{54\,600}{4}\left(\frac{1.57}{0.79}\right)^2$$

$$K = 53\,600 \text{ lb/ft/strut}$$

$$K = 799 \text{ newtons/mm/strut}$$

These strut-body elastic properties were incorporated into the analysis and the resulting calculated stability boundaries are identified by the term elastic-shock-absorber theory. As a matter of interest, it may be noted that 65 percent of the elastic energy associated with the effective spring of the upper strut is stored in the body; the remainder, in the strut and shock absorbers. Sixty percent of the elastic energy under the effective spring curve for the lower strut is attributable to body elasticity.

When the simplified method of including elasticity in the analysis is considered, the elastic-shock-absorber theory shown in figure 11 follows the experimental trends extremely well including the sharp decline in the boundary at $\psi_s \approx 10^o$. This much improved prediction capability is contrary to what one might intuitively assume in view of the small amount of energy stored in the model during impact. With the shock absorber forces and spring forces in series, the maximum potential energy stored in each leg assembly is approximately 0.75 ft-lb (1.017 joule) or enough to lift the vehicle only 0.0139 ft (0.004 m).

Vertical landings on 10^o slope.- Analytically and experimentally determined landing stability boundaries for vertical landings on a 10^o slope are presented in figure 14. The

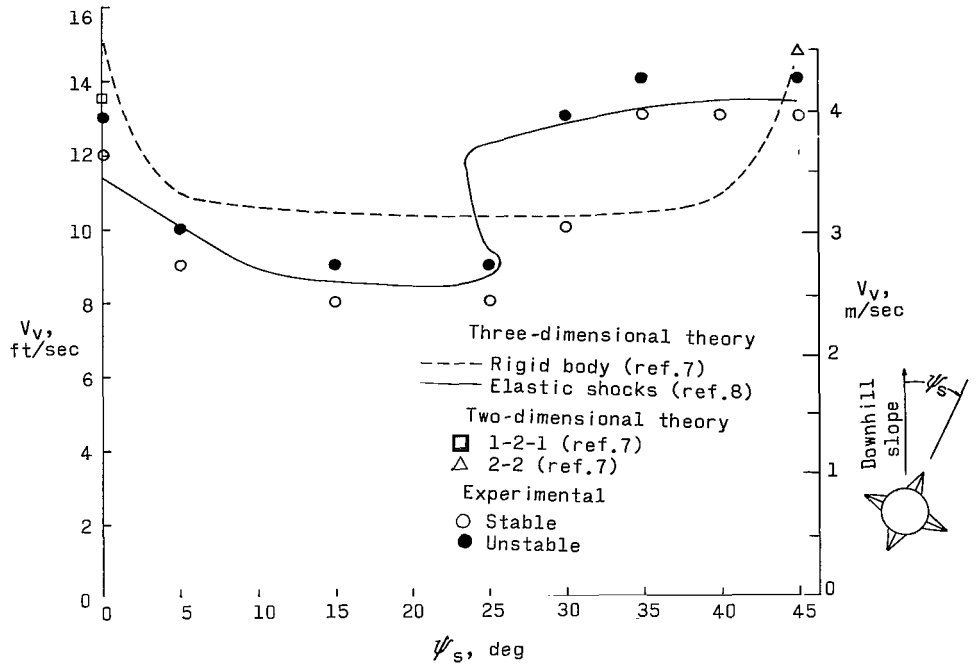

Figure 14.- Experimental and analytical stability profile-vertical velocity as a function of yaw orientation relative to direction of slope. $\sigma = 10^0$; $V_h = 0$.

boundary predicted by the rigid-body theory is generally of the correct magnitude; however, it does not follow the trends of the experiment. Transition points for the 1-2-1, 1-0-1, and 2-2 modes of overturning were manually computed by the two-dimensional, inelastic impact theory of reference 7. The 1-2-1 and 2-2 transition points are shown at $\psi_s = 0^o$ and $\psi_s = 45^o$, respectively. Again, the 1-0-1 transition point was much higher than any other point in the figure and is not shown. The boundary computed from the inelastic-shock-absorber theory is not shown in the figure since only stable conditions were predicted for impact velocities up to 20 ft/sec (6.096 m/sec). At these high impact velocities, considerable stroking of the shock absorbers essentially allows the landing gear to conform to the landing slope. In the rigid-body theory, on the other hand, much of the pre-impact translational momentum of the model is transformed at impact into rotational momentum which yields a much lower stability boundary. The elastic-shock-absorber representation of the model yielded boundaries which are in excellent agreement with the model tests at all values of ψ_s. It is important to note that again, the inclusion of measured strut-body elastic characteristics in the mathematical model produced dramatic improvement in the predicted stability characteristics.

The relatively good correlation between the rigid-body theory and experiment as compared with the complete lack of correlation between inelastic shock absorber theory and experiment may be misleading. One could erroneously conclude that for rough-cut

calculations, the rigid-body theory is adequate. This conclusion is not generally true. It appears that the stabilizing effect of the shock absorbers is offset by the destabilizing effects of the vehicle elasticity. Therefore, one must assume that the apparent adequacy of the rigid-body theory is accidental.

Landing with forward velocity on 10^{o} slope.- In figure 15, computed and measured landing stability boundaries are plotted for impacts with a 5 ft/sec (1.52 m/sec) horizontal velocity component. The vertical velocity required to overturn the model is presented as a function of the cross-slope angle α_s.

For cross-slope angles less than 50^{o}, the rigid-body theory and the inelastic-shock-absorber theory predict boundaries which are in close agreement with each other but fall generally above the experimental boundary. In the region $50^{o} < \alpha_s \leq 90^{o}$ both the rigid-body and inelastic-shock-absorber boundaries are rather erratic and generally unconservative. As was the case with the previously discussed landing conditions, the elastic shock-absorber theory predicts stability boundaries which are in much better agreement with experiment than do the other two mathematical models. However, the correlations in this instance are not as good as those obtained for the cases in which the horizontal velocity was zero. It should be noted that for $0^{o} < \alpha_s < 45^{o}$, the initial contact with the landing surface is made by the trailing foot whereas at $\alpha_s > 45^{o}$ the side foot impacts first.

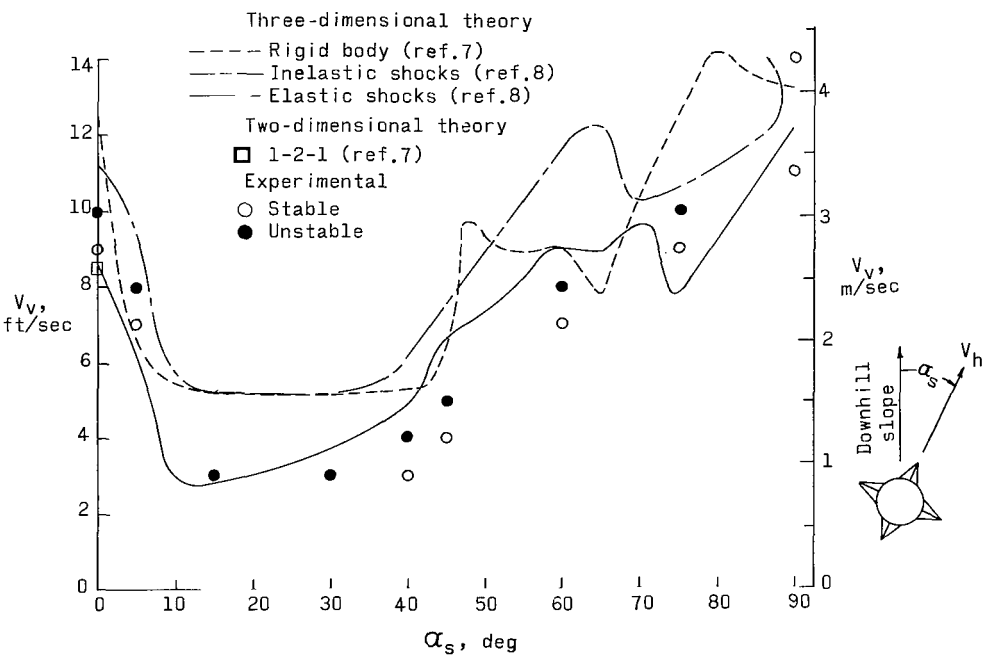

Figure 15.- Experimental and analytical stability profile-vertical velocity as a function of cross-slope angle. $\sigma = 10^{o}$; $V_h = 5$ ft/sec (1.74 m/sec).

CONCLUSIONS

A 1/6-scale dynamic model of a lunar module (LM) type of spacecraft has been tested to determine the overturning stability boundaries. Analytical stability boundaries have been determined for a rigid nondeformable model, a rigid model with shock absorbers, and an elastic model with shock absorbers. Examination of the experimentally determined stability boundaries and correlation of these boundaries with those predicted by each of the three analytical simulations led to the following conclusions:

1. Landing approaches which result in three-dimensional tumbling can impose much more severe limitations on landing-approach velocities than do those in which the tumbling motion is two dimensional.

2. The symmetric 1-2-1 landing can be less stable than the symmetric 2-2 landing.

3. The addition of horizontal velocity results in a decrease in stability.

4. Relatively small amounts of stored elastic energy can significantly influence the landing stability of lunar-module-type vehicles.

5. Load-limiting shock absorbers generally tend to improve vehicle stability characteristics.

6. For both vertical and cross-slope landing approaches, the analysis which includes the gross vehicle elastic properties as well as the shock absorber characteristics predicts the post-impact tumbling stability boundaries with reasonable accuracy over the complete range of model yaw attitudes.

7. Both the rigid-body theory and the inelastic-shock-absorber analysis yield stability boundaries which are generally nonconservative.

8. The excellent correlation between the experiment and the elastic-shock-absorber theory tends to validate the mathematical procedures employed and the approximations made in NASA Technical Note D-4216.

Langley Research Center,
National Aeronautics and Space Administration,
Langley Station, Hampton, Va., May 8, 1967,
124-08-04-13-23.

REFERENCES

1. Alper, Joel R.: Landing Dynamics – A Survey of STL State-of-the-Art and Recommendations for Further Investigations. EM 13-5,9758-6001-RU-000, Space Technology Labs., Inc., Jan. 1963.

2. Anon.: Summary Report of Lunar Landing Dynamics Systems Investigation. Rept. No. MM-64-10 (Dept. 870), Bendix Products Aerospace Div., Bendix Corp., Oct. 1964.

3. Sala, R.: Plan for Landing Gear Stability Drop Tests – 1/6-Scale Model. LTP-560-1 (Contract NAS 9-1100), Grumman Aircraft Engineering Corp., Apr. 8, 1963.

4. Blanchard, Ulysse J.: Characteristics of a Lunar Landing Configuration Having Various Multiple-Leg Landing-Gear Arrangements. NASA TN D-2027, 1964.

5. Donroe, F.: Results of Landing Gear Stability Drop Tests 1/6-Scale Model. LTR 904-16001 (Contract NAS 9-1100), Grumman Aircraft Engineering Corp., Sept. 6, 1963.

6. Black, Raymond J.: Quadrupedal Landing Gear Systems for Spacecraft. J. Spacecraft, vol. 1, no. 2, Mar.-Apr. 1964, pp. 196-203.

7. Walton, W. C., Jr.; Herr, R. W.; and Leonard, H. W.: Studies of Touchdown Stability for Lunar Landing Vehicles. J. Spacecraft, vol. 1, no. 5, Sept.-Oct. 1964, pp. 552-556.

8. Walton, William C., Jr.; and Durling, Barbara J.: A Procedure for Computing the Motion of a Lunar-Landing Vehicle During the Landing Impact. NASA TN D-4216, 1967.

NASA-Langley, 1967 —— 31 L-4771

"The aeronautical and space activities of the United States shall be conducted so as to contribute . . . to the expansion of human knowledge of phenomena in the atmosphere and space. The Administration shall provide for the widest practicable and appropriate dissemination of information concerning its activities and the results thereof."

—NATIONAL AERONAUTICS AND SPACE ACT OF 1958

NASA SCIENTIFIC AND TECHNICAL PUBLICATIONS

TECHNICAL REPORTS: Scientific and technical information considered important, complete, and a lasting contribution to existing knowledge.

TECHNICAL NOTES: Information less broad in scope but nevertheless of importance as a contribution to existing knowledge.

TECHNICAL MEMORANDUMS: Information receiving limited distribution because of preliminary data, security classification, or other reasons.

CONTRACTOR REPORTS: Scientific and technical information generated under a NASA contract or grant and considered an important contribution to existing knowledge.

TECHNICAL TRANSLATIONS: Information published in a foreign language considered to merit NASA distribution in English.

SPECIAL PUBLICATIONS: Information derived from or of value to NASA activities. Publications include conference proceedings, monographs, data compilations, handbooks, sourcebooks, and special bibliographies.

TECHNOLOGY UTILIZATION PUBLICATIONS: Information on technology used by NASA that may be of particular interest in commercial and other non-aerospace applications. Publications include Tech Briefs, Technology Utilization Reports and Notes, and Technology Surveys.

Details on the availability of these publications may be obtained from:

SCIENTIFIC AND TECHNICAL INFORMATION DIVISION

NATIONAL AERONAUTICS AND SPACE ADMINISTRATION

Washington, D.C. 20546